

Theoretical Prediction of Two-Dimensional Functionalized MXene Nitrides as Topological Insulators

Yunye Liang,^{1,*} Mohammad Khazaei,² Ahmad Ranjbar,² Masao Arai,³ Seiji Yunoki,^{2,4,5} Yoshiyuki Kawazoe,^{6,7} Hongming Weng,^{8,9} and Zhong Fang^{8,9}

¹*Department of Physics, Shanghai Normal University, Shanghai 200234, China*

²*Computational Materials Science Research Team,
RIKEN Advanced Institute for Computational
Science (AICS), Kobe, Hyogo 650-0047, Japan*

³*International Center for Materials Nanoarchitectonics,
National Institute for Materials Science (NIMS),
1-1 Namiki, Tsukuba 305-0044, Ibaraki, Japan*

⁴*Computational Condensed Matter Physics Laboratory,
RIKEN, Wako, Saitama 351-0198, Japan*

⁵*Computational Quantum Matter Research Team,
RIKEN Center for Emergent Matter Science (CEMS), Wako, Saitama 351-0198, Japan*

⁶*New Industry Creation Hatchery Center,
Tohoku University, Sendai, 980-8579, Japan*

⁷*Department of Physics and Nanotechnology, SRM University,
Katankulathur, Chennai 603203, Tamil Nadu, India*

⁸*Beijing National Laboratory for Condensed Matter Physics,
and Institute of Physics, Chinese Academy of Sciences, Beijing 100190, China*

⁹*Collaborative Innovation Center of Quantum Matter, Beijing, China*

(Dated: October 15, 2018)

Abstract

Recently, two-dimensional (2D) transition metal carbides and nitrides, namely, MXenes have attracted lots of attention for electronic and energy storage applications. Due to a large spin-orbit coupling (SOC) and the existence of a Dirac-like band at the Fermi energy, it has been theoretically proposed that some of the MXenes will be topological insulators (TIs). Up to now, all of the predicted TI MXenes belong to transition metal carbides, whose transition metal atom is W, Mo or Cr. Here, on the basis of first-principles and \mathbb{Z}_2 index calculations, we demonstrate that some of the MXene nitrides can also be TIs. We find that $\text{Ti}_3\text{N}_2\text{F}_2$ is a 2D TI, whereas $\text{Zr}_3\text{N}_2\text{F}_2$ is a semimetal with nontrivial band topology and can be turned into a 2D TI when the lattice is stretched. We also find that the tensile strain can convert $\text{Hf}_3\text{N}_2\text{F}_2$ semiconductor into a 2D TI. Since Ti is one of the mostly used transition metal element in the synthesized MXenes, we expect that our prediction can advance the future application of MXenes as TI devices.

I. INTRODUCTION

At the beginning, graphene was proposed as a two-dimensional (2D) topological insulator (TI)¹⁻⁷. Unfortunately, the band gap of graphene is too tiny to be measured experimentally. Later on, the observation of topological quantum states (TQs) was realized in a 2D quantum well of HgTe/CdTe^{8,9}. This experimental achievement boosted the quick rising of the field of TIs. For example, the idea of band topology was extended to three-dimensional (3D) systems and other symmetry protected TQs¹⁰⁻¹⁴. Recently, the band topology in metals,¹⁵ including the topological Dirac semimetal¹⁶⁻¹⁹, Weyl semimetal²⁰⁻²⁶, and node-line semimetal²⁷⁻³⁰ has also been intensively studied. Many of materials with TQs were firstly predicted by theoretical calculations before the experimental confirmations^{7,31}. 2D TIs are particularly useful in applications because they are expected to host quantum spin Hall effect (QSHE) with one-dimensional helical edge states. The electrons in such edge states have opposite velocities in opposite spin channels, and thus the backscattering is prohibited as long as the perturbation does not break the time-reversal symmetry. Such helical edge states are expected to serve as “two-lane highway” for dissipationless electron transport, which promises great potential application in low-power and multi-functional spintronic devices.

Compared with the number of well characterized 3D TI materials, fewer 2D TIs have been experimentally discovered^{7,32}. The quantum wells of HgTe/CdTe⁹ and InAs/GaSb³³ are among the well-known experimentally confirmed 2D TIs. The requirements of precise control of molecular beam epitaxy growth and operation at ultra-low temperatures make further studies hard for the possible applications. Different methods are used to find or create prospective TIs, for examples, by tuning the band gaps through the strength of spin-orbit coupling (SOC) in graphene-like honeycomb lattice structures, such as the low-buckled silicene³⁴, chemically decorated single layer honeycomb lattice of Sn³⁵, Ge³⁶, Bi, or Sb³⁷, and bucked square lattice BiF³⁸, or by examining new 2D systems, which might be exfoliated from the 3D layered structural materials, such as ZrTe₅, HfTe₅^{39,40}, Bi₄Br₄, and Bi₄I₄^{41,42}. Transition-metal dichalcogenide⁴³⁻⁴⁷ and square-octagon haeckelite⁴⁸⁻⁵⁰ structure belong to the later category. Among these proposals, ZrTe₅, HfTe₅, Bi₄Br₄, Bi₄I₄, WTe₂ and Bismuthene on SiC substrate seem to be very promising.⁵¹

MXenes are a novel family of 2D transition metal carbonitrides⁵²⁻⁵⁴ which have been recently obtained by the selective chemical etching of MAX phases — M_{n+1}AX_n ($n=1-$

3), where M, A, and X are a transition metal, an element of group 13-14, and C or N, respectively⁵⁵. MXenes have some unique properties and applications^{56,57}. As examples, it is predicted that MXenes can be used as energy storage devices such as batteries and electrochemical supercapacitors^{58,59}. This is because a variety of cations with various charges and sizes, including Na^+ , K^+ , NH_4^+ , Mg^{2+} , and Al^{3+} , can be easily intercalated into the exfoliated MXenes⁵⁸.

The flexibility of MXenes make them prospective candidates of the wearable energy storage devices⁶⁰. The bare surfaces of MXene sheets are chemically active and are usually terminated with atoms or chemical groups, depending on the synthesis process, usually fluorine (F), oxygen (O), or hydroxyl (OH)⁶¹⁻⁶³. Up to now, many 2D MXenes such as Ti_2C , V_2C , Nb_2C , Mo_2C , Ti_3CN , Ti_3C_2 , Ta_4C_3 , and Ti_3C_2 have been experimentally produced^{53,54,64,65}. More recently, double ordered transition metals MXenes, Mo_2TiC_2 and $\text{Mo}_2\text{Ti}_2\text{C}_3$, have also been synthesized^{66,67}.

Various 2D MXenes have been predicted to be TIs. In this regard, we have reported that the functionalized MXenes with oxygen, M_2CO_2 (M=W, Mo, and Cr) are 2D TIs.⁶⁸ The results are robust against the use of different exchange-correlation functional approximations. The bulk band gap of W_2CO_2 is as large as 0.194 eV within generalized gradient approximation (GGA)⁶⁹⁻⁷¹ and is enhanced to 0.472 eV within non-local Heyd-Scuseria-Ernzerhof (HSE06) hybrid functional^{72,73}. TIs can also be found in ordered double transition metals $\text{M}'_2\text{M}''\text{C}_2$ MXenes, where $\text{M}'=\text{Mo}$ and W , and $\text{M}''=\text{Ti}$, Zr , and Hf ⁷⁴⁻⁷⁶. A 2D TI with large band gap is crucial to realize the long-sought-for topological superconductivity and Majorana modes through proximity effect^{6,77}. Inspired by these findings, we have studied a large number of 2D MXenes in order to obtain new TI candidates with different topologically nontrivial properties that may be easily synthesized^{55,78}. The possible variants of 2D MXenes are achieved by replacing O^{2-} by F^- or $(\text{OH})^-$ ^{61,62,79}, substituting transition-metal M, varying C with N or B⁷⁸, and tuning the number of layers n in MXene M_{n+1}C_n ^{80,81}. Properly tailoring materials with a single or any combination of the above may lead to more and better 2D topologically insulating MXenes.

In this paper, by using first-principles calculations, we predict that functionalized MXenes $\text{Ti}_3\text{N}_2\text{F}_2$ and $\text{Zr}_3\text{N}_2\text{F}_2$ have nontrivial band topology: the former is a 2D TI and the latter is a semimetal which can be turned into a 2D TI by the tensile strain. We also predict that $\text{Hf}_3\text{N}_2\text{F}_2$ semiconductor can be converted into TI by the tensile strain. The stabilities of the

structures are confirmed by phonon dispersion calculations. The band inversion, which is crucial to the nontrivial band topology, is found to occur among the different combinations of d -orbitals due to the crystal field effect. The results are robust against different exchange-correlation functional approximations such as the GGA and the HSE06 hybrid functional.

The rest of this paper is organized as follows. First, the computational details are briefly summarized in Sec. II. The main results together with discussion are provided in Sec. III. Finally, the paper is concluded in Sec. IV.

II. COMPUTATIONAL DETAILS

Calculations are performed by Vienna *ab initio* simulation package (VASP), within the Perdew-Burke-Ernzerhof (PBE) version of the GGA functional for exchange correlation^{69–71}. The SOC is taken into account self-consistently. The cut-off energy is 520 eV for plane wave expansion. The optimization calculations are done with $12 \times 12 \times 1$ k-point sampling grid. The crystal structures are fully relaxed until the residual forces on each atom become less than 0.001 eV/Å. A vacuum space between layers is 40 Å, in order to minimize the interactions between the layer with its periodic images. PHONOPY is employed to calculate the phonon dispersion⁸². Considering the possible underestimation of band gap within the GGA, the non-local HSE06 hybrid functional^{72,73} is further applied to check the band topology. To explore the edge states, we apply the Green’s function method⁷ based on the tight-binding model with the maximally localized Wannier functions (MLWFs)^{83,84} of d orbitals of Ti and p orbitals of N and F as the basis set. The MLWFs are generated by using the software package OpenMX^{85,86}.

III. RESULTS AND DISCUSSION

A. Atomic Structure

The bare MXenes are chemically reactive. Hence, depending on the synthesis process, the transition metals on the surfaces of the MXenes are functionalized by a mixture of F, O, and OH. First-principles calculations show that the electronic properties of MXenes can be engineered by appropriate surface functionalization^{56,61,62,87}. The MXenes with full surface

functionalizations, namely, two chemical groups on both sides of the surfaces, are thermodynamically more favorable than those with the partial functionalizations⁶¹. Figures 1(a) and 1(b) show the crystal structure of functionalized MXene $\text{Ti}_3\text{N}_2\text{F}_2$, which consists of seven atomic layers with hexagonal lattice, including three Ti layers, two N layers, and two F layers.

As shown in Fig. 1(b), the chemical functional groups can occupy possibly three different sites, indicated by A, B, and T, on each surface. Therefore, there are six structurally possible configurations which should be considered, as listed in Table I. The atomic positions and lattice vectors for these six different configurations are fully optimized and the total energies of the optimized structures are summarized in Table I. The calculations reveal that the MXene with BB-type fluorine functionalization has the lowest energy.

The space group of BB-type $\text{Ti}_3\text{N}_2\text{F}_2$ is $P\bar{3}m1$, and there are two inequivalent types of Ti atoms: the inner Ti atomic layer and the outer Ti atomic layers. The Wyckoff position of the inner Ti atom is $1a$ and it is the origin of the primitive cell. The Wyckoff position of the outer Ti atoms is $2d$ and the corresponding coordinates are $(1/3, 2/3, z)$ and $(1/3, 2/3, \bar{z})$.

Since there is no report of the successful experimental synthesis of 2D $\text{Ti}_3\text{N}_2\text{F}_2$ in the literatures yet, the phonon dispersion spectrum of the BB structure is calculated to confirm the structural stability. As shown in Fig. 1(c), all phonon frequencies are positive, indicating that the structure is dynamically stable.

B. Electronic Structure of $\text{Ti}_3\text{N}_2\text{F}_2$

Next, we examine the electronic structure of $\text{Ti}_3\text{N}_2\text{F}_2$ with the optimized atomic structure obtained above. As shown in Fig. 2(a), if the SOC is not considered, the lowest conduction band and the highest valence band touch each other at the Γ point exactly at the Fermi energy. They are two-fold degenerate and characterized by the irreducible representation E_g . The PBE calculations with the SOC show in Fig. 2(b) that $\text{Ti}_3\text{N}_2\text{F}_2$ may be semimetal with slightly having compensated electron and hole Fermi pocket. However, as shown in Fig. 2(b), the more accurate calculations using HSE06 with the SOC show that $\text{Ti}_3\text{N}_2\text{F}_2$ is an insulator.

Given the fact that the primitive cell of $\text{Ti}_3\text{N}_2\text{F}_2$ possesses the inversion symmetry and

TABLE I. The total energies (in eV per unit cell) for the six possible configurations of $M_3N_2F_2$, where M is Ti, Zr, and Hf. In each unit cell, fluorine atoms on both surfaces are required for full surface saturations. T, A, and B indicate three different absorption positions, as indicated in Fig. 1(b). All calculations here are performed within GGA and without spin polarization. The energy of the most favorable structure (BB) is set to zero.

sites of Fluorine	Ti ₃ N ₂ F ₂	Zr ₃ N ₂ F ₂	Hf ₃ N ₂ F ₂
TT	1.667	2.119	1.761
AA	0.093	0.388	0.634
TB	1.025	1.072	0.886
TA	0.873	1.256	1.226
BB	0	0	0
BA	0.090	0.234	0.379

following the method proposed by Fu and Kane¹², the topological invariant ν reads as

$$\delta(k_i) = \prod_{n=1}^N \xi_n(k_i); \quad (-1)^\nu = \prod_{i=1}^4 \delta(k_i) \quad (1)$$

where $\xi_n(k_i)$ is +1 (-1) for even (odd) parity of the n th occupied band (not including the Kramers degenerate partner) at time reversal invariant momentum k_i , and N is the number of occupied bands (counting only one of the Kramers degenerate pairs). Since Ti₃N₂F₂ possesses a hexagonal lattice, the time reversal invariant momenta k_i are the Γ point at $\mathbf{k}=(0,0,0)$ and the three M points at $\mathbf{k}=(0,0.5,0)$, $(0.5,0,0)$, and $(0.5,0.5,0)$. Investigating the parities of the occupied bands at the Γ and M points, we find that $\delta(\Gamma) = -1$ and $\delta(M) = 1$, and thus the \mathbb{Z}_2 invariant ν is 1. Therefore, we can conclude that Ti₃N₂F₂ is a 2D TI with a band gap as large as 0.05 eV within the HSE06 calculation.

The band inversion plays an important role in the nontrivial band topology. As we will discuss in the following, the band inversion in Ti₃N₂F₂ is not ascribed to the SOC. To shed light on it, the projected band structures onto d orbitals of different Ti atoms without the SOC is shown in Fig. 3. Here, we only consider d orbitals of Ti atoms because the bands near the Fermi energy are composed mostly of these d orbitals. In Ti₃N₂F₂, two inequivalent Ti atoms have different local symmetries. The symmetry of the inner Ti atom is D_{3d} , while the symmetry of the two outer Ti atoms is C_{3v} . According to the point symmetry of the crystal

lattice, five d orbitals of Ti atoms are split. As shown in Fig 3, different combinations of d orbitals lead to different parities. For example, at the Γ point, the band labeled with A_{1g} in Fig. 2(a) stems from the d_{z^2} orbitals of inner Ti atom and outer ones. Due to the inversion symmetry, the d_{z^2} orbitals of the outer Ti atoms are combined symmetrically to form a band with even parity. The band with A_{2u} symmetry at the Γ point possesses odd parity. Therefore, the d orbitals of the inner Ti atom with D_{3d} symmetry does not contribute to this state because the inversion center is located at the inner Ti atom and the d orbitals have only the even parity. It is merely the antisymmetric combination of the d_{z^2} orbitals of the outer Ti atoms that contributes to this state. On the other hand, d_{xy} and $d_{x^2-y^2}$ orbitals of the three Ti atoms result into two-fold degenerate E_g bands at the Γ point near the Fermi energy [see Figs. 2(a) and 3]. As discussed in the following, the band inversion occurs at the Γ point among the bands with A_{2u} and E_g symmetries, leading to $\delta(\Gamma) = -1$. In contrast, there is no band inversion at the M point. As shown in Fig. 2(b), the SOC is important only to open the gap at the Γ point. The similar band inversion mechanism was found in W_2CO_2 ⁶⁸ and double transition metals $M'_2M''C_2$ ($M' = Mo, W$; $M'' = Ti, Zr, Hf$) MXenes⁷⁵.

It is known that the order of energy bands may change upon applying strain to convert TIs into trivial insulators and vice versa^{35,36,74}. Next, we calculate the energy bands of $Ti_3N_2F_2$ in the presence of compressive and stretching strain. For simplicity, we assume that the space group does not change with the strain, but the corresponding atomic structures are fully optimized. Figure 4(a) shows the results when the lattice constant is compressed by 12%. We find that the band with A_{2u} symmetry at the Γ point shift downwards in energies upon increasing the compressive strain, and eventually it becomes occupied and locates below the bands with E_g symmetry at $\sim 10\%$ of the compressive strain [see Fig.4(c)]. This implies that the topological property of the energy bands changes greatly because $\delta(\Gamma) = 1$.

As shown in Fig. 4(b), when the lattice is stretched about 12%, we find a Dirac-like dispersion with the Dirac point at the Fermi energy along the Σ axis (the axis connecting the Γ and M points). This Dirac point is due to the accidental degeneracy⁷⁹ and indeed the SOC opens the gap as large as 0.02 eV [see Fig. 4(d)]. The point group along the Σ axis is C_s , whose symmetry is lower than the symmetry at the Γ point. According to the compatibility relation, the doubly degenerate bands with E_g symmetry at the Γ point is split into non-degenerate bands with A' and A'' symmetries along the Σ axis, where the band with A'' symmetry is higher in energy than that with A' symmetry, as shown in Fig. 4(b).

Note also that the energy band with A_{1g} symmetry at the Γ point becomes the band with A' symmetry along the Σ axis. The stretching of the lattice moves the band with A_{1g} symmetry upwards and, around 5% stretching, its energy becomes higher than that of the bands with E_g symmetry, as shown in Fig. 4(c). At the same time, the A' band, originating from the A_{1g} band at the Γ point, crosses the A'' band, branched off from the E_g bands at the Γ point, along the Σ axis, forming the Dirac point at the Fermi energy. As shown in Fig. 4(d), the SOC lifts this accidental degeneracy by opening the gap. Since the A_{1g} and E_g bands have the same parity, the exchange of their ordering does not change the topological property, and $\text{Ti}_3\text{N}_2\text{F}_2$ is still a TI.

Finally, the edge states of $\text{Ti}_3\text{N}_2\text{F}_2$ nanoribbon are studied. The nanoribbon is made by cutting it along the a axis [see Fig. 1(a)]. Figure 5 summarizes the results of the electronic band structures. It is clearly observed in Fig. 5 that the emergent edge states cross the Fermi energy five times (i.e., odd number of times), revealing a non-trivial topology of the state.

C. Electronic Properties of $\text{Zr}_3\text{N}_2\text{F}_2$ and $\text{Hf}_3\text{N}_2\text{F}_2$

Since Zr and Hf atoms have very similar physical and chemical properties with Ti atom, next we study the electronic structures of $\text{Zr}_3\text{N}_2\text{F}_2$ and $\text{Hf}_3\text{N}_2\text{F}_2$, and their responses to the applied strain.

The energy bands of $\text{Zr}_3\text{N}_2\text{F}_2$ without and with the SOC are shown in Figs. 6(a) and 6(b), respectively. $\text{Zr}_3\text{N}_2\text{F}_2$ is semimetal with having compensated electron and hole Fermi pockets. However, since the topmost and bottommost bands around the Fermi energy do not cross their bands, we can still calculate the \mathbb{Z}_2 invariant ν for bands denoted by black solid lines in Fig. 6(b), and find that ν is 1. Therefore, $\text{Zr}_3\text{N}_2\text{F}_2$ has the same band topology as $\text{Ti}_3\text{N}_2\text{F}_2$. If the lattice is compressed as large as 3%, indicated by the red arrow in Fig. 6(e), the band with A_{2u} symmetry at the Γ point becomes lower in energy than the bands with E_g symmetry [see Fig. 6(c) for the energy band under 5% compression]. As a result, the band topology changes because $\delta(\Gamma)$ is now +1.

On the other hand, if it is stretched, the band with A_{1g} symmetry at the Γ point moves upward in energy, whereas the bands with E_g symmetry moves downward, and the order of these bands is eventually exchanged when the stretch strain exceeds 4% [indicated by the

blue arrow in Fig. 6(e)]. At the same time, the Dirac-like dispersion appears along the Σ axis. For example, the band structure with 7% stretching is shown in Fig. 6(d). This is analogous to the case of $\text{Ti}_3\text{N}_2\text{F}_2$ discussed above. The accidental degeneracy of the Dirac point is lifted by introducing the SOC and thus the stretched $\text{Zr}_3\text{N}_2\text{F}_2$ becomes a TI. For instance, in the case of 7% stretching, the SOC opens the band gap as large as 0.05 eV [see Fig. 6(f)].

The energy band of $\text{Hf}_3\text{N}_2\text{F}_2$ is shown in Fig. 7. As opposed to $\text{Ti}_3\text{N}_2\text{F}_2$, we find that $\text{Hf}_3\text{N}_2\text{F}_2$ is a trivial insulator because the band with A_{2u} symmetry at the Γ point is occupied, while the bands with E_g symmetry is unoccupied [see Fig. 7(a)]. However, by applying the stretching strain as large as 5%, the band inversion occurs among the bands with A_{2u} and E_g symmetries. As shown in Fig. 7(b), the band with A_{2u} symmetry shifts upwards and becomes unoccupied, whereas the bands with E_g symmetry are now the valence bands. Therefore, the stretched $\text{Hf}_3\text{N}_2\text{F}_2$ has a nontrivial band topology. The band gap opens in the presence of SOC and can be as large as 0.1 eV within the HSE06 calculations with 5% of the stretching strain [see Fig. 7(c)].

D. The stabilities with the tensile strains

To confirm the stabilities of $\text{Ti}_3\text{N}_2\text{F}_2$, $\text{Zr}_3\text{N}_2\text{F}_2$ and $\text{Hf}_3\text{N}_2\text{F}_2$ in the presence of different tensile strains, it is straightforward to calculate their phonon spectra, respectively. The calculated phonon spectra are shown in Fig. 8. We find that these compressed and stretched structures can be stable in the range as we have discussed previously, because they have all positive frequencies. Our results are consistent with the measurements that MXene flakes are highly flexible materials with excellent tensile and compressive strengths^{58,88}. However, for $\text{Ti}_3\text{N}_2\text{F}_2$, we plotted the result with 8.5% stretching in Fig. 8(d), and one phonon branch, as indicated by the arrow, underwent a drop to the low frequency at K point. By further stretching, $\text{Ti}_3\text{N}_2\text{F}_2$ is not stable because the vibrational branch with imaginary frequencies can be found.

The modulation of the tensile strain in experiments is still a challenge. Different methods and techniques have been proposed to realize it. For example, the tensile tests were performed by gluing MXene films onto supporting paper frames⁸⁸. It is reported that by introducing polyvinyl alcohol (PVA) films, the tensile strength was improved significantly⁸⁸.

However, the experimental observation of our prediction with different tensile strains is still an open question.

IV. CONCLUSIONS

Previously, we have proposed that the functionalized transition metal carbides M_2CO_2 ($M=W, Mo, \text{ and } Cr$) and $M'_2M''C_2$ ($M'= Mo, W; M''= Ti, Zr, Hf$) are 2D TIs^{68,75}. Based on the first-principles calculations, here we have found that the topological property can be extended to functionalized nitride MXenes, such as $Ti_3N_2F_2$ and $Zr_3N_2F_2$. Although $Hf_3N_2F_2$ is a trivial insulator, it can be converted into a TI by strain. Their response to the strain indicates that these materials are promising candidates as future nano devices and strain sensors. Because of the easier production process by a selective chemical etching method, hosting QSHE at ambient condition, the high stability and antioxidant upon exposure to air, and consisting of environmental friendly elements, we expect that our finding will stimulate further experimental studies.

V. ACKNOWLEDGMENTS

Y.L. would like to express his sincere thanks to the crew in the Center for Computational Materials Science of the Institute for Materials Research, Tohoku University, for their continuous support of the SR16000 supercomputing facilities. M.K and A.R are grateful to RIKEN Advanced Center for Computing and Communication (ACCC) for the allocation of computational resource of the RIKEN supercomputer system (HOKUSAI GreatWave). Part of the calculations in this study were performed on Numerical Materials Simulator at NIMS. M.K. gratefully acknowledges the support by Grant-in-Aid for Scientific Research (No. 17K14804) from MEXT Japan.

* liangyunye@shnu.edu.cn

¹ C. L. Kane and E. J. Mele, *Phys. Rev. Lett.* **95**, 146802 (2005).

² C. L. Kane and E. J. Mele, *Phys. Rev. Lett.* **95**, 226801 (2005).

³ B. A. Bernevig and S.-C. Zhang, *Phys. Rev. Lett.* **96**, 106802 (2006).

- ⁴ Y. Yao, F. Ye, X.-L. Qi, S.-C. Zhang, and Z. Fang, *Phys. Rev. B* **75**, 041401 (2007).
- ⁵ M. Z. Hasan and C. L. Kane, *Rev. Mod. Phys.* **82**, 3045 (2010).
- ⁶ X.-L. Qi and S.-C. Zhang, *Rev. Mod. Phys.* **83**, 1057 (2011).
- ⁷ Hongming Weng, Xi Dai, and Zhong Fang, *MRS Bulletin* **39**, 849 (2014).
- ⁸ B. A. Bernevig, T. L. Hughes, and S.-C. Zhang, *Science* **314**, 1757 (2006).
- ⁹ M. König, S. Wiedmann, C. Brüne, A. Roth, H. Buhmann, L. W. Molenkamp, X.-L. Qi, and S.-C. Zhang, *Science* **318**, 766 (2007).
- ¹⁰ L. Fu, C. L. Kane, and E. J. Mele, *Phys. Rev. Lett.* **98**, 106803 (2007).
- ¹¹ J. E. Moore and L. Balents, *Phys. Rev. B* **75**, 121306 (2007).
- ¹² L. Fu and C. L. Kane, *Phys. Rev. B* **76**, 045302 (2007).
- ¹³ R. Roy, *Phys. Rev. B* **79**, 195321 (2009).
- ¹⁴ C.-K. Chiu, J. C. Y. Teo, A. P. Schnyder, and S. Ryu, *Rev. Mod. Phys.* **88**, 035005 (2016).
- ¹⁵ H. Weng, X. Dai, and Z. Fang, *J. Phys.: Condens. Matter.* **28**, 303001 (2016).
- ¹⁶ Z. Wang, Y. Sun, X.-Q. Chen, C. Franchini, G. Xu, H. Weng, X. Dai, and Z. Fang, *Phys. Rev. B* **85**, 195320 (2012).
- ¹⁷ Z. Wang, H. M. Weng, Q. Wu, X. Dai, and Z. Fang, *Phys. Rev. B* **88**, 125427 (2013).
- ¹⁸ Z. K. Liu, B. Zhou, Y. Zhang, Z. J. Wang, H. Weng, D. Prabhakaran, S.-K. Mo, Z. X. Shen, Z. Fang, X. Dai, Z. Hussain, and Y. L. Chen, *Science* **343**, 864 (2014).
- ¹⁹ Z. K. Liu, J. Jiang, B. Zhou, Z. J. Wang, Y. Zhang, H. M. Weng, D. Prabhakaran, S. K. Mo, H. Peng, P. Dudin, T. Kim, M. Hoesch, Z. Fang, X. Dai, Z.-X. Shen, D. L. Feng, Z. Hussain, and Y. L. Chen, *Nature Materials* **13**, 677 (2014).
- ²⁰ X. Wan, A. M. Turner, A. Vishwanath, and S. Y. Savrasov, *Phys. Rev. B* **83**, 205101 (2011).
- ²¹ G. Xu, H. M. Weng, Z. Wang, X. Dai, and Z. Fang, *Phys. Rev. Lett.* **107**, 186806 (2011).
- ²² S. M. Huang et al. *Nature Communications* **6**, 7373 (2014).
- ²³ H. M. Weng, C. Fang, Z. Fang, B. A. Bernevig, and X. Dai, *Phys. Rev. X* **5**, 011029 (2015).
- ²⁴ B. Q. Lv, H. M. Weng, B. B. Fu, X. P. Wang, H. Miao, J. Ma, P. Richard, X. C. Huang, L. X. Zhao, G. F. Chen, Z. Fang, X. Dai, T. Qian, and H. Ding, *Phys. Rev. X* **5**, 031013 (2015).
- ²⁵ B. Q. Lv, N. Xu, H. M. Weng, J. Z. Ma, P. Richard, X. C. Huang, L. X. Zhao, G. F. Chen, C. Matt, F. Bisti, V. Strokov, J. Mesot, Z. Fang, X. Dai, T. Qian, M. Shi, and H. Ding, *Nature Physics* **11**, 724 (2015).

- ²⁶ S. Y. Xu, I. Belopolski, N. Alidoust, M. Neupane, G. Bian, C. Zhang, R. Sankar, G. Chang, Z. Yuan, C.-C. Lee, S.-M. Huang, H. Zheng, J. Ma, D. S. Sanchez, B. K. Wang, A. Bansil, F. Chou, P. P. Shibayev, H. Lin, S. Jia, and M. Z. Hasan, *Science* **349**, 613617 (2015).
- ²⁷ A. A. Burkov, M. D. Hook, and Leon Balents. *Phys. Rev. B* **84**, 235126 (2011).
- ²⁸ H. Weng, Y. Liang, Q. Xu, R. Yu, Z. Fang, X. Dai, and Y. Kawazoe, *Phys. Rev. B* **92**, 045108 (2015).
- ²⁹ Y. Kim, B. J. Wieder, C. L. Kane, and A. M. Rappe, *Phys. Rev. Lett.* **115**, 036806 (2015).
- ³⁰ R. Yu, H. Weng, Z. Fang, X. Dai, and X. Hu, *Phys. Rev. Lett.* **115**, 036807 (2015).
- ³¹ H. Zhang and S.-C. Zhang. *Physica Status Solidi (RRL) - Rapid Research Letters* **7**, 72 (2013).
- ³² Y. Ando, *J. Phys. Soc. Jpn.* **82**, 102001 (2013).
- ³³ I. Knez, R.-R. Du, and G. Sullivan, *Phys. Rev. Lett.* **107**, 136603 (2011).
- ³⁴ C.-C. Liu, W. Feng, and Y. Yao, *Phys. Rev. Lett.* **107**, 076802 (2011).
- ³⁵ Y. Xu, B. Yan, H.-J. Zhang, J. Wang, G. Xu, P. Tang, W. Duan, and S.-C. Zhang, *Phys. Rev. Lett.* **111**, 136804 (2013).
- ³⁶ C. Si, J. Liu, Y. Xu, J. Wu, B.-L. Gu, and W. Duan, *Phys. Rev. B* **89**, 115429 (2014).
- ³⁷ Z. Song, C.-C. Liu, J. Yang, J. Han, M. Ye, B. Fu, Y. Yang, Q. Niu, J. Lu, and Y. Yao, *NPG Asia Materials* **6**, 147 (2014).
- ³⁸ W. Luo and H. Xiang, *Nano Letters* **15**, 3230 (2015).
- ³⁹ H. Weng, X. Dai, and Z. Fang, *Phys. Rev. X* **4**, 011002 (2014).
- ⁴⁰ R. Wu, J.-Z. Ma, S.-M. Nie, L.-X. Zhao, X. Huang, J.-X. Yin, B.-B. Fu, P. Richard, G.-F. Chen, Z. Fang, X. Dai, H. M. Weng, T. Qian, H. Ding, and S. H. Pan, *Phys. Rev. X* **6**, 021017 (2016).
- ⁴¹ J.-J. Zhou, W. Feng, C.-C. Liu, S. Guan, and Y. Yao, *Nano Letters* **14**, 4767 (2014).
- ⁴² G. Aut̃Áls, A. Isaeva, L. Moreschini, J. C. Johannsen, A. Pisoni, R. Mori, W. Zhang, T. G. Filatova, A. N. Kuznetsov, L. Forr̃Aş, W. Van den Broek, Y. Kim, K. S. Kim, A. Lanzara, J. D. Denlinger, E. Rotenberg, A. Bostwick, M. Grioni, and O. V. Yazyev, *Nature Materials* **15**, 154 (2016).
- ⁴³ X. Qian, J. Liu, L. Fu, and J. Li, *Science* **346**, 1344 (2014).
- ⁴⁴ F. Zheng, C. Cai, S. Ge, X. Zhang, X. Liu, H. Lu, Y. Zhang, J. Qiu, T. Taniguchi, K. Watanabe, S. Jia, J. Qi, J.-H. Chen, D. Sun and J. Feng, *Adv. Mater.* **4845**, (2016).
- ⁴⁵ H. Xiang, B. Xu, J. Liu, Y. Xia, H. Lu, J. Yin and Z. Liu, *AIP Advances* **6**, 075008, (2016).

- ⁴⁶ Z. Fei, T. Palomaki, S. Wu, W. Zhao, X. Cai, B. Sun, P. Nguyen, J. Finney, X. Xu, D. H. Cobden, *Nature Physics* **13**, 677 (2017).
- ⁴⁷ S. Tang, C. Zhang, D. Wong, Z. Pedramrazi, H-Z. Tsai, C. Jia, B. Moritz, M. Claassen, H. Pyu, S. Kahn, J. Jiang, H. Yan, M. Hashimoto, D. Lu, R. G. Moore, C. Hwang, C. Hwang, Z. Hussain, Y. Chen, M. M. Ugeda, Z. Liu, X. Xie, T. P. Devereaux, M. F. Crommie, S-K, Mo, Z-X. Shen, *Nature Physics* **13**, 683 (2017).
- ⁴⁸ S. M. Nie, Z. Song, H. Weng, and Z. Fang, *Phys. Rev. B* **91**, 235434 (2015).
- ⁴⁹ Y. Ma, L. Kou, X. Li, Y. Dai, S. C. Smith, and T. Heine, *Phys. Rev. B* **92**, 085427 (2015).
- ⁵⁰ Y. Sun, C. Felser, and B. Yan, *Phys. Rev. B* **92**, 165421 (2015).
- ⁵¹ F. Reis, G. Li, L. Dudy, M. Bauernfeind, S. Glass, W. Hanke, R. Thomale, J. Schäfer, and R. Claessen, *Science* **357**, 287 (2017).
- ⁵² M. Naguib, M. Kurtoglu, V. Presser, J. Lu, J. Niu, M. Heon, L. Hultman, Y. Gogotsi, and M. W. Barsoum, *Adv. Mater.* **23**, 4248 (2011).
- ⁵³ M. Naguib, O. Mashtalir, J. Carle, V. Presser, J. L., L. Hultman, Y. Gogotsi, and M. W. Barsoum, *ACS Nano* **6**, 1322 (2011).
- ⁵⁴ M. Naguib, V. N. Mochalin, M. W. Barsoum, and Y. Gogotsi, *Adv. Mater.* **26**, 992 (2014).
- ⁵⁵ M. W. Barsoum, *Progress in Solid State Chemistry* **28**, 201 (2000).
- ⁵⁶ M. Khazaei, A. Ranjbar, M. Arai, T. Sasaki, and S. Yunoki, *J. Mater. Chem. C* **5**, 2488 (2017).
- ⁵⁷ B. Anasori, M. R. Lukatskaya, and Y. Gogotsi, *Nat. Rev.* **1**, 16098 (2017).
- ⁵⁸ M. R. Lukatskaya, O. Mashtalir, C. E. Ren, Y. Dall’Agnese, P. Rozier, P. L. Taberna, M. Naguib, P. Simon, M. W. Barsoum and Y. Gogotsi, *Science* **341**, 1502 (2013).
- ⁵⁹ O. Mashtalir, M. Naguib, V. N. Mochalin, Y. Dall’Agnese, M. Heon, M. W. Barsoum and Y. Gogotsi, *Nature Communications* **4**, 1716 (2013).
- ⁶⁰ J. R. Miller, *Science* **335**, 1312 (2012).
- ⁶¹ M. Khazaei, M. Arai, T. Sasaki, C.-Y. Chung, N. S. Venkataramanan, M. Estili, Y. Sakka, and Y. Kawazoe, *Adv. Funct. Mater.* **23**, 2185 (2013).
- ⁶² M. Khazaei, M. Arai, T. Sasaki, M. Estili, and Y. Sakka, *Phys. Chem. Chem. Phys.* **16**, 7841 (2014).
- ⁶³ K. J. Harris, M. Bugnet, M. Naguib, M. W. Barsoum, and G. R. Goward, *J. Phys. Chem. C* **119**, 13713 (2015).

- ⁶⁴ M. Naguib, O. Mashtalir, M. R. Lukatskaya, B. Dyatkin, C. Zhang, V. Presser, Y. Gogotsi and M. W. Barsoum, *Chem. Comm.* **50**, 7420 (2014).
- ⁶⁵ R. Meshkini, L. -Å. Näslund, J. Halim, *Scr. Mater.* **108**, 147 (2015).
- ⁶⁶ B. Anasori, Y. Xie, M. Beidaghi, J. Lu, B. C. Hosler, L. Hultman, P. R. C. Kent, Y. Gogotsi, and M. W. Barsoum, *ACS Nano* **9**, 9507 (2016).
- ⁶⁷ B. Anasori, C. Shi, E. J. Moon, Y. Xie, C. A. Voigt, P. R. C. Kent, S. J. May, S. J. L. Billinge, M. W. Barsoum, and Y. Gogotsi, *Nanoscale Horiz.* **1**, 227 (2016).
- ⁶⁸ H. Weng, A. Ranjbar, Y. Liang, Z. Song, M. Khazaei, S. Yunoki, M. Arai, Y. Kawazoe, Z. Fang, X. Dai, *Phys. Rev. B* **92**, 075436 (2015).
- ⁶⁹ G. Kresse and J. Furthmüller, *Computational Materials Science* **6**, 15 (1996).
- ⁷⁰ G. Kresse and J. Furthmüller, *Phys. Rev. B* **54**, 11169 (1996).
- ⁷¹ J. P. Perdew, K. Burke, and M. Ernzerhof, *Phys. Rev. Lett.* **77**, 3865 (1996).
- ⁷² J. Heyd, G. E. Scuseria, and M. Ernzerhof, *J. Chem. Phys.* **118**, 8207 (2003).
- ⁷³ J. Heyd, G. E. Scuseria, and M. Ernzerhof, *J. Chem. Phys.* **124**, 219906 (2006).
- ⁷⁴ C. Si, K-H, Jin, J. Zhou, Z. Sun, and F. Liu, *Nano. Lett.* **16**, 6584 (2016).
- ⁷⁵ M. Khazaei, A. Ranjbar, M. Arai and S. Yunoki, *Phys. Rev. B* **94**, 125152 (2016).
- ⁷⁶ L. Li, *Computational Materials Science* **124**, 8 (2016).
- ⁷⁷ L. Fu and C. L. Kane, *Phys. Rev. Lett.* **100**, 096407 (2008).
- ⁷⁸ M. Khazaei, M. Arai, T. Sasaki, M. Estili and Y. Sakka, *J. Phys.: Condens Matt* **26**, 505503 (2014).
- ⁷⁹ H. Fashandi, V. Ivády, P. Eklund, and A. L. Spetz, M. I. Katsnelson, and I. A. Abrikosov, *Phys. Rev. B* **92**, 155142 (2015).
- ⁸⁰ M. Khazaei, M. Arai, T. Sasaki, M. Estili and Y. Sakka, *Sci. Technol. Adv. Mater.* **15**, 014208 (2014).
- ⁸¹ X. Wang, X. Shen, Y. Gao, Z. Wang, R. Yu and L. Chen, *J. Am. Chem. Soc.* **137**, 2715 (2015).
- ⁸² A. Togo, F. Oba, and I. Tanaka, *Phys. Rev. B* **78**, 134106 (2008).
- ⁸³ N. Marzari and D. Vanderbilt, *Phys. Rev. B* **56**, 12847 (1997).
- ⁸⁴ I. Souza, N. Marzari, and D. Vanderbilt, *Phys. Rev. B* **65**, 035109 (2001).
- ⁸⁵ <http://www.openmx-square.org>.
- ⁸⁶ H. Weng, T. Ozaki, and K. Terakura, *Phys. Rev. B* **79**, 235118 (2009).

- ⁸⁷ M. Khazaei, M. Arai, T. Sasaki, A. Ranjbar, Y. Liang, and S Yunoki, *Phys. Rev. B* **92**, 075411 (2015).
- ⁸⁸ Z. Ling, C. E. Ren, M-Q Zhao, J. Yang, J. M. Giammarco, J. Qiu, M. W. Barsoum, and Y. Gogotsi, *Proc. Natl Acad. Sci. USA* **111**, 16676 (2014).

Captions

- : FIG. 1 (a) Top and (b) side views of optimized crystal structure of $\text{Ti}_3\text{N}_2\text{F}_2$. Here, Ti, N, and F atoms are represented by light blue, dark blue, and red spheres, respectively. Three possible positions, i.e., B (on top of N atom), T (on top of Ti atom in the outer layer), and A (on top of Ti atom in the central layer), decorating either side of the surfaces are shown in (b). The unit cell (black solid lines) with primitive lattice vectors \vec{a} and \vec{b} are indicated in (a). (c) The phonon dispersion spectrum for optimized $\text{Ti}_3\text{N}_2\text{F}_2$.

- : FIG. 2 The energy bands (solid lines) of $\text{Ti}_3\text{N}_2\text{F}_2$ calculated using the PBE functional (a) without and (b) with the SOC. The energy bands calculated using the hybrid HSE06 functional with the SOC are also shown by dashed lines in (b). E_F is the Fermi energy. The irreducible representations of the energy bands at the Γ point close to the Fermi energy are indicated in (a). (c) A schematic figure of the band inversion mechanism in $\text{Ti}_3\text{N}_2\text{F}_2$. The d type atomic orbitals (AOs) are split due to the crystal field (CF) of lattice with $P\bar{3}m1$ symmetry. Band inversion (BI) occurs between states with different parities.

- : FIG. 3 The projected energy bands onto d orbitals of (a) two outer and (b) inner Ti atoms for $\text{Ti}_3\text{N}_2\text{F}_2$ calculated using the PBE functional without the SOC. E_F is the Fermi energy.

- : FIG. 4 The energy bands of $\text{Ti}_3\text{N}_2\text{F}_2$ under the strain calculated using the PBE functional without the SOC. (a) The lattice is compressed by 12%. (b) The lattice is stretched by 12%. The red circle indicates the Dirac point in (b). The irreducible representations of the energy bands at the Γ points and along the Σ axis (the axis connecting the Γ and M points) near the Fermi energy E_F are indicated. (c) The energy evolution of three bands at the Γ point with A_{1g} , A_{2u} , and E_g symmetries, indicated in (a) and (b), when the lattice is compressed (negative strain) or stretched (positive strain). The red arrow indicates the compressive strain above which the band with A_{2u} symmetry becomes lower in energy than that with E_g symmetry, and thus the system becomes topologically trivial. The blue arrow implies the stretching strain above which the accidental degeneracy along the Σ axis occurs. (d) The enlarged energy bands indicated

by the red circles in (b). The accidental degeneracy at the Dirac point is lifted with the introduction of the SOC (red lines).

- : FIG. 5 The edge states of $\text{Ti}_3\text{N}_2\text{F}_2$ cut along the a axis [see Fig. 1(a)]. The Fermi energy is located at zero energy. The inset shows the enlarged energy bands around the \bar{X} point. It is clearly observed that the edge states cross the Fermi energy five times and are doubly degenerate at the \bar{X} point.

- : FIG. 6 The energy bands of $\text{Zr}_3\text{N}_2\text{F}_2$ with no strain (a) in the absence of SOC and (b) in the presence of SOC, and with (c) 5% compression and (d) 7% stretching in the absence of SOC. The irreducible representations of the energy bands at the Γ point near the Fermi energy E_F are indicated. (e) The energy evolution of the bands at the Γ point with A_{2u} , A_{1g} , and E_g symmetries. The red and blue arrows imply the occurrence of bands crossing with varying the strain. (f) The enlarged energy bands (black lines) indicated by the red circle in (d). The accidental degeneracy at the Dirac point is lifted with the SOC (red lines). All calculations are performed using the PBE functional.

- : FIG. 7 The energy bands of $\text{Hf}_3\text{N}_2\text{F}_2$ calculated using the HSE06 hybrid functional (a) without any strain and the SOC, (b) with 5% stretching strain but no SOC, and (c) with 5% stretching strain and the SOC. The irreducible representations of the energy bands at the Γ point near the Fermi energy E_F are indicated.

- : FIG. 8 The phonon spectra of $\text{Ti}_3\text{N}_2\text{F}_2$, $\text{Zr}_3\text{N}_2\text{F}_2$ and $\text{Hf}_3\text{N}_2\text{F}_2$ with different tensile strains.

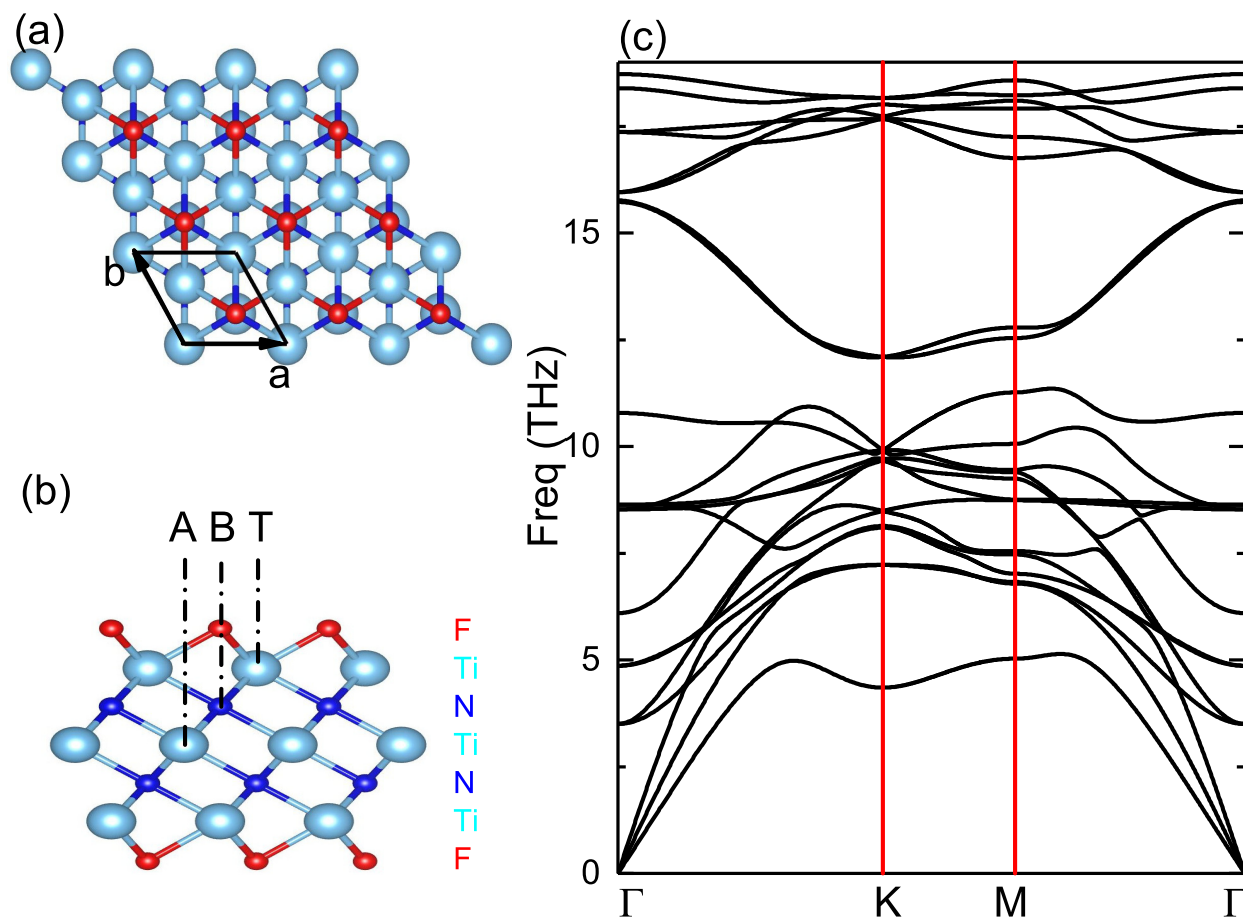


FIG. 1. Y. Liang *et. al.*

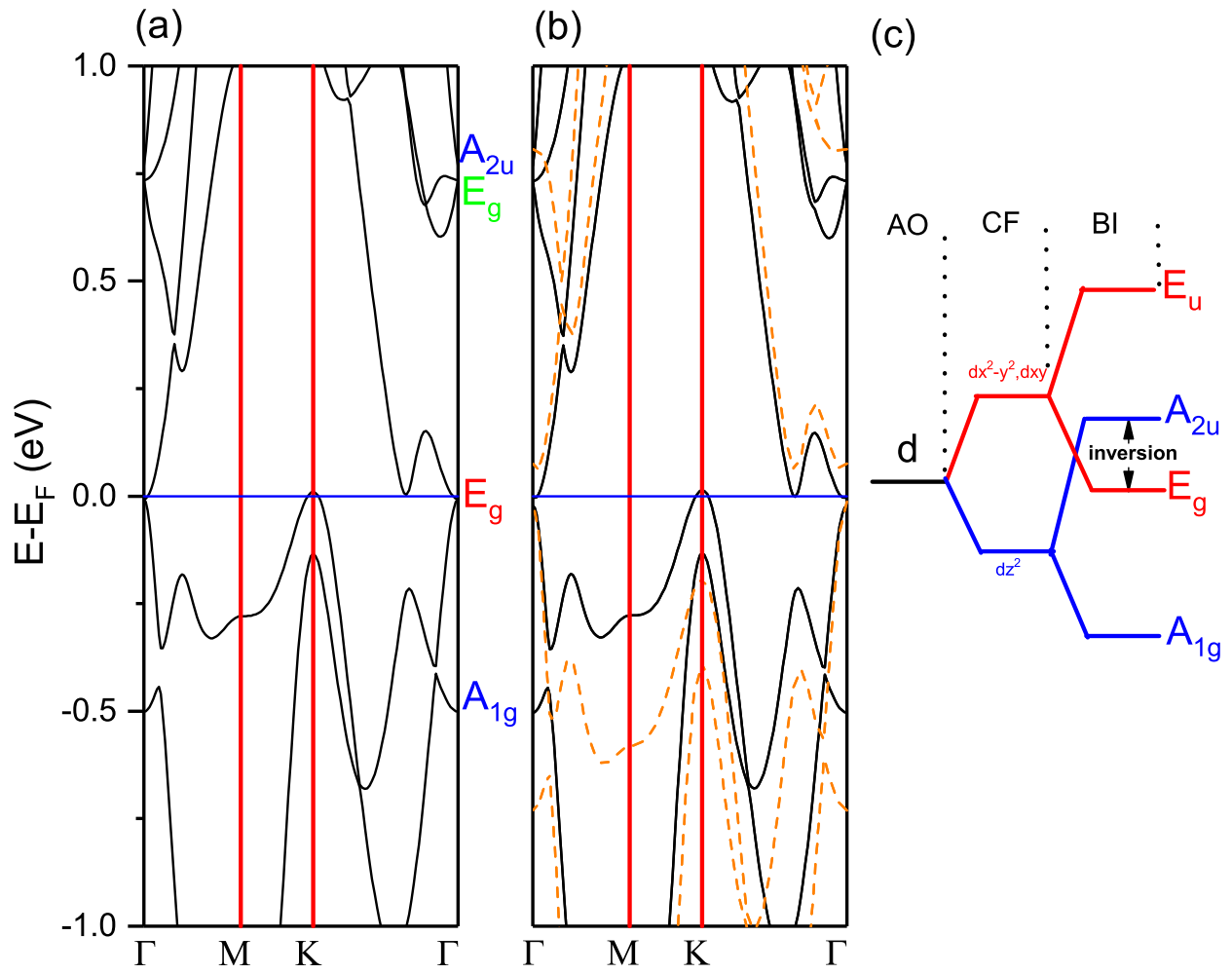


FIG. 2. Y. Liang *et. al.*

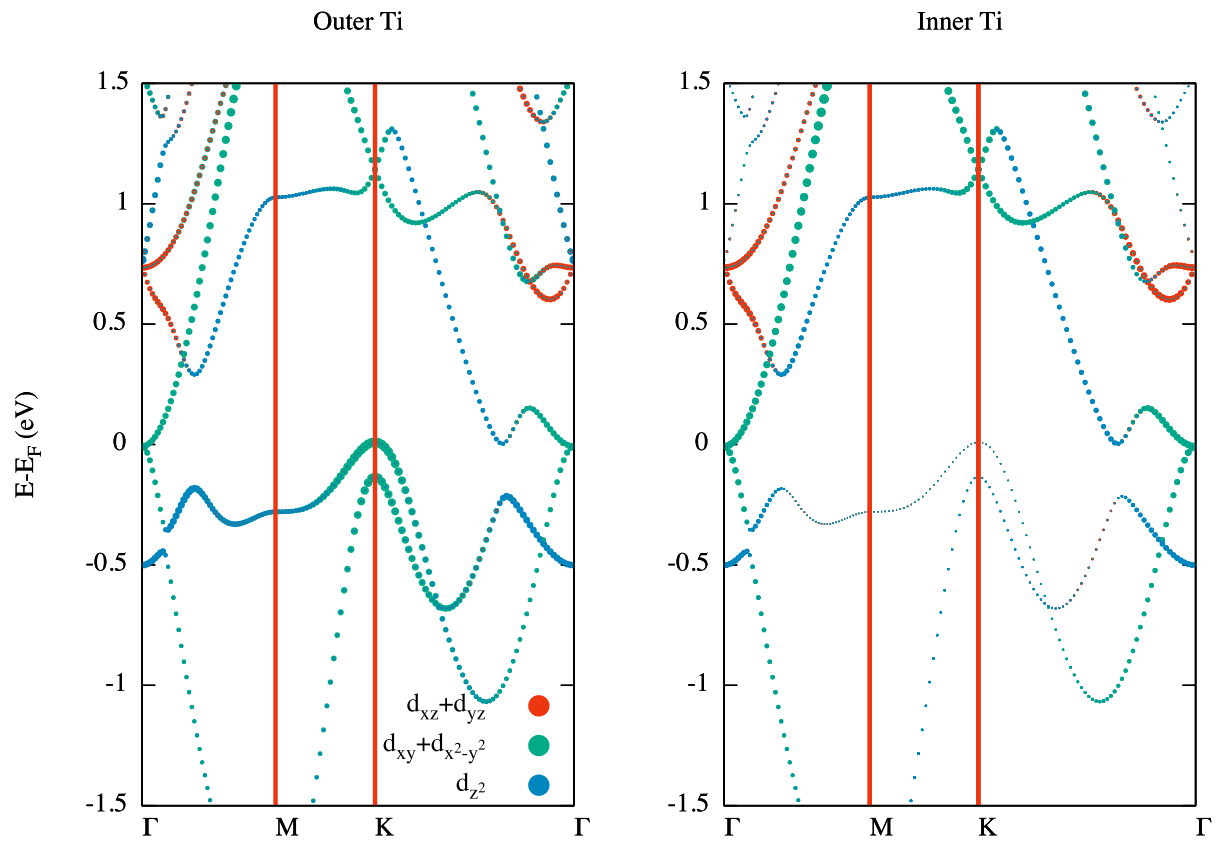


FIG. 3. Y. Liang *et. al.*

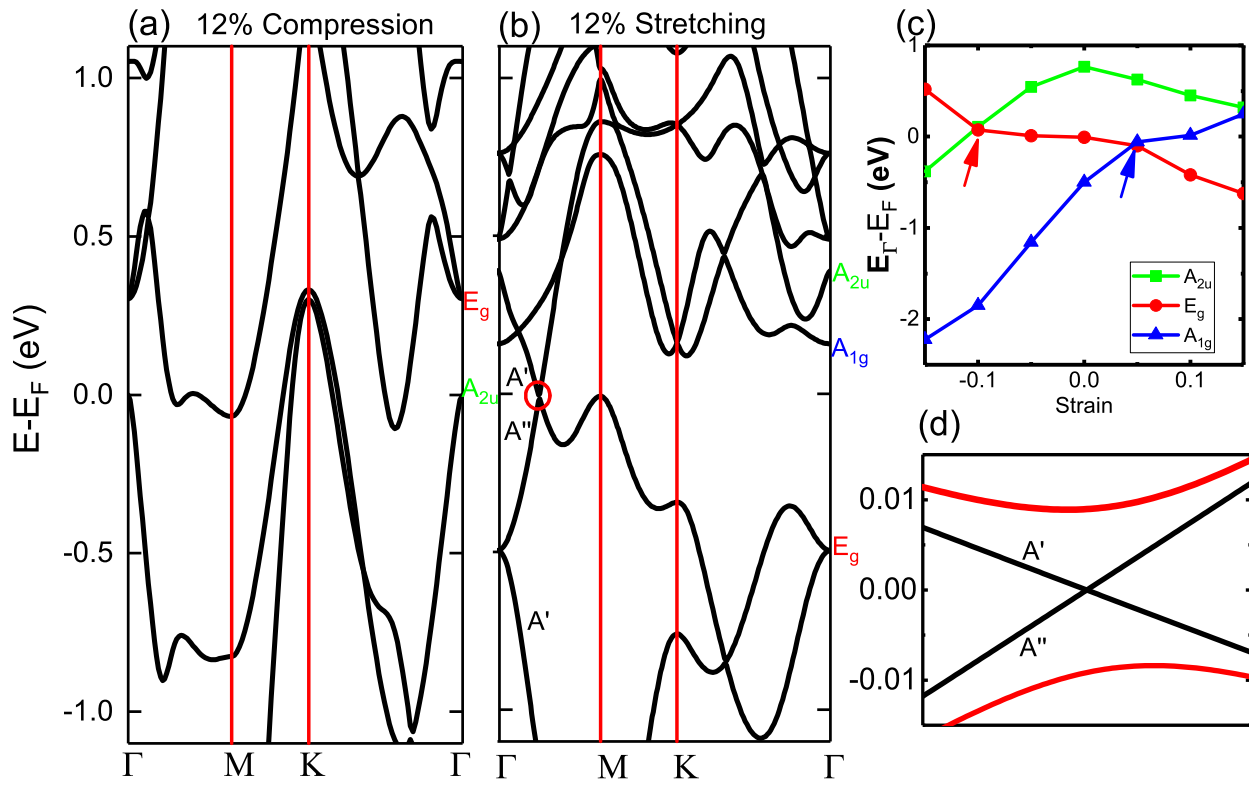


FIG. 4. Y. Liang *et. al.*

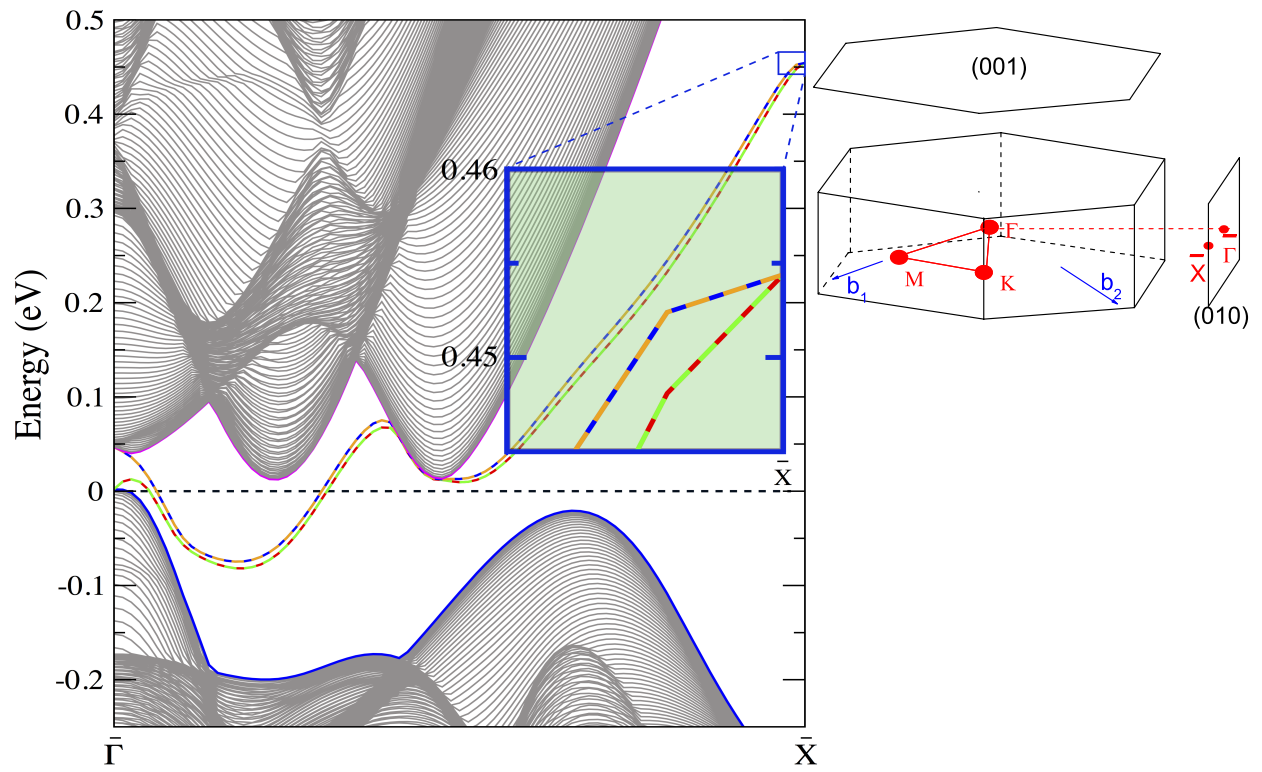


FIG. 5. Y. Liang *et. al.*

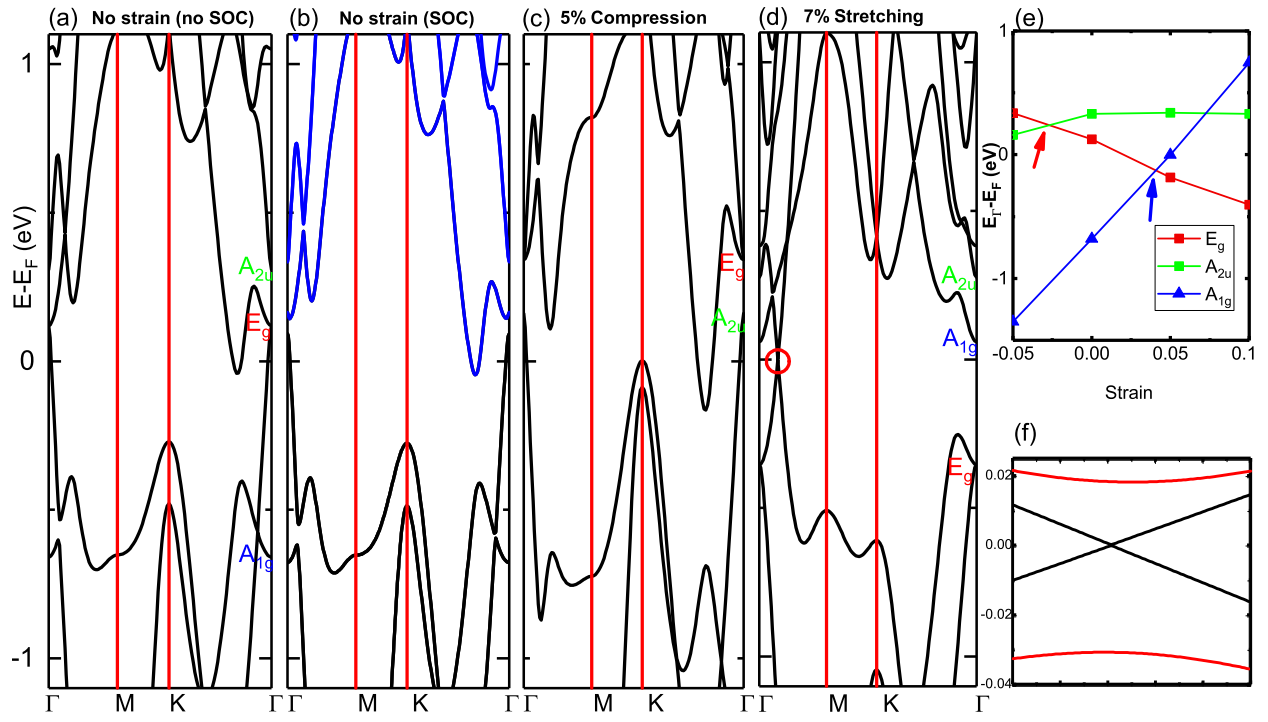


FIG. 6. Y. Liang *et. al.*

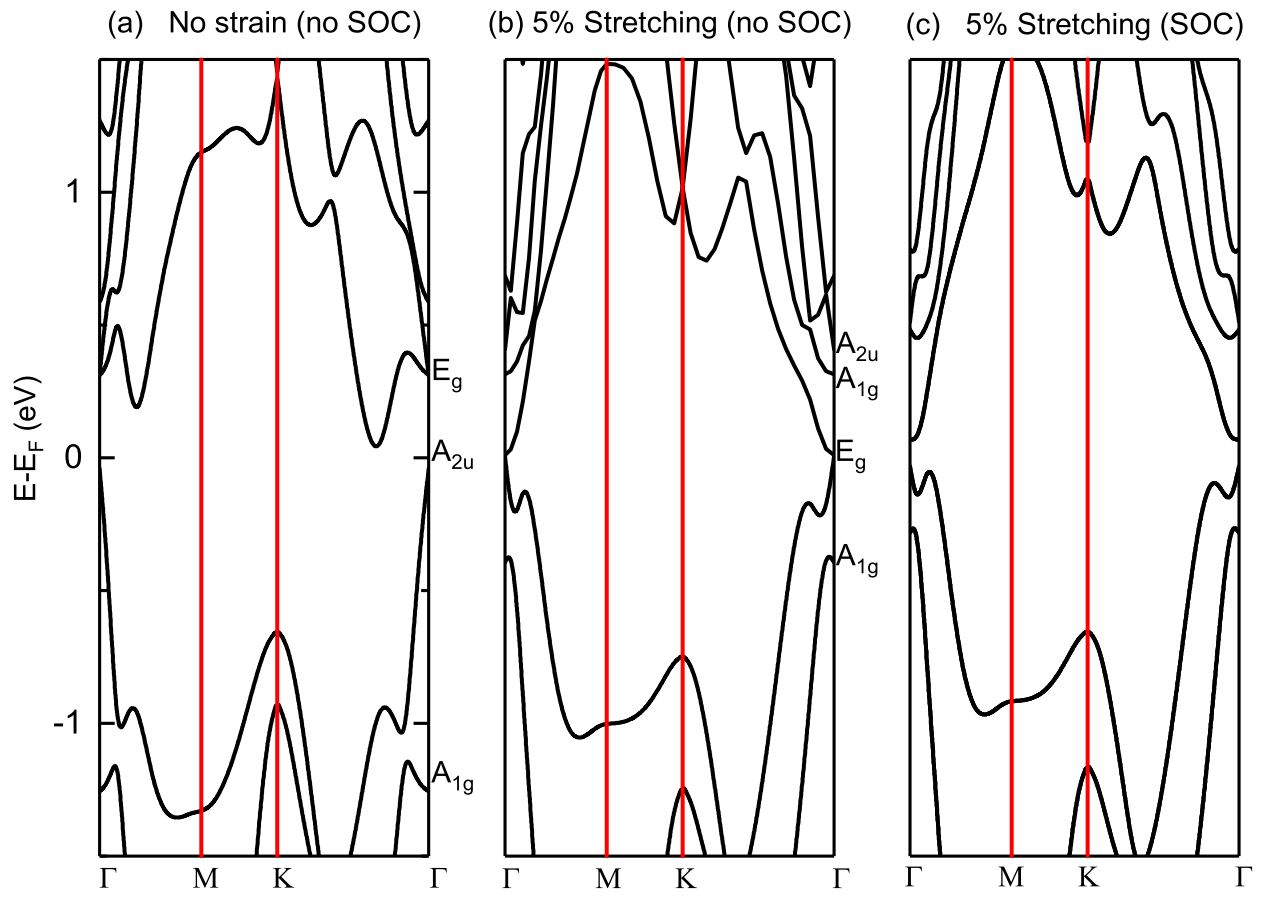


FIG. 7. Y. Liang *et. al.*

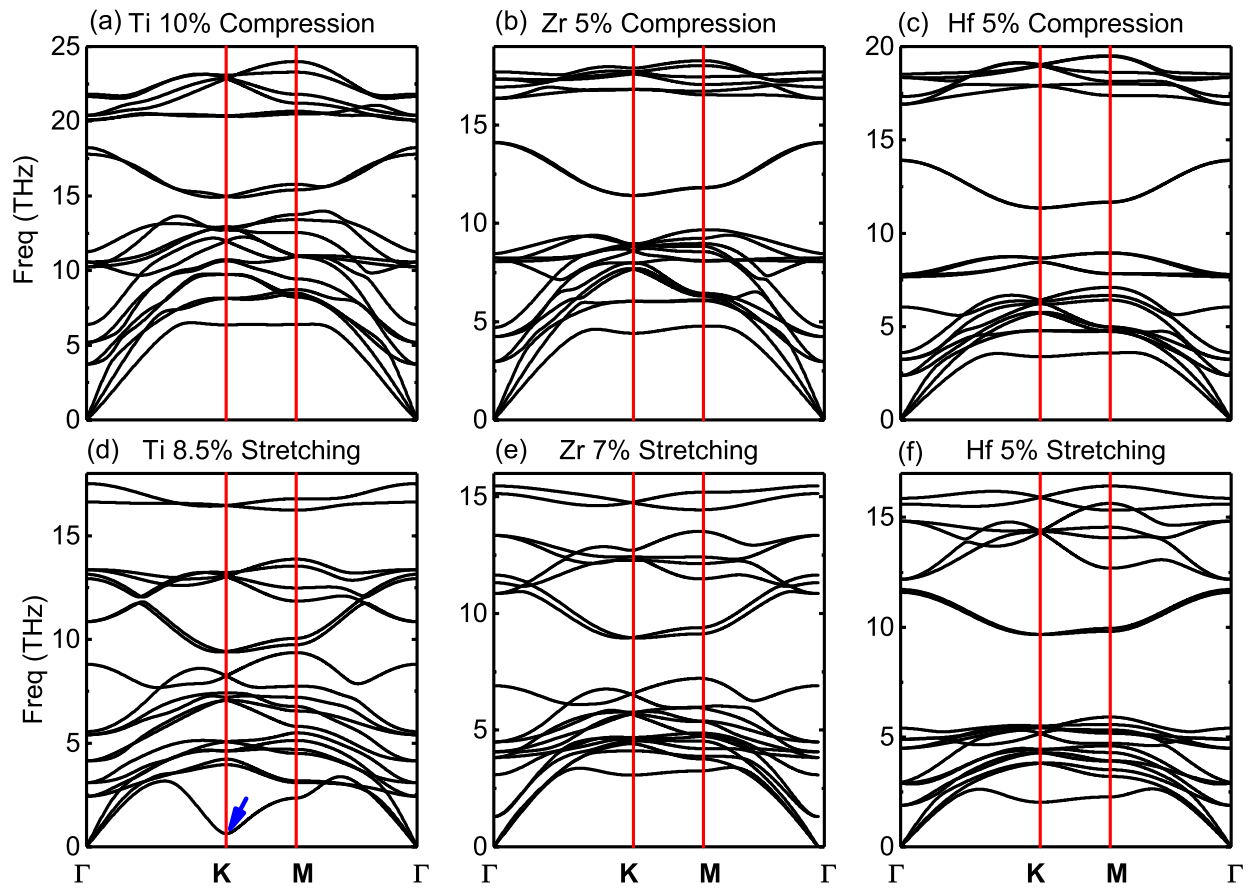


FIG. 8. Y. Liang *et. al.*